Stress relaxation in polymeric microlattice materials

CrossMark

Sebastian Krödel[a,c], Lichen Li[b], Andrei Constantinescu[b], Chiara Daraio[c,*]

[a] Department of Mechanical and Process Engineering, Swiss Federal Institute of Technology (ETH), Zürich, Switzerland
[b] Laboratoire de Mécanique des Solides, CNRS UMR7649, Ecole Polytechnique, 91128 Palaiseau Cedex, France
[c] Engineering and Applied Science, California Institute of Technology, Pasadena, CA 91125, USA

ARTICLE INFO

ABSTRACT

Breakthroughs in fabrication techniques enabled the creation of microlattice materials, which are assembled from truss-like elements on the micro-scale. The mechanical properties of these materials can be controlled varying the geometry of their microstructure. Here, we study the effect of topology and effective density on the visco-elastic properties of microlattices fabricated by direct laser writing. We perform micro scale relaxation experiments using capacitive force sensing in compression. The experimental results are analyzed using a generalized Maxwell model and the viscoelastic properties are studied in terms of density scaling laws. We develop a finite element model that allows extracting the bulk polymer viscoelastic properties. The experimental results show that the stiffness of lattice materials can be adjusted independently from the loss factor in a wide range of frequencies. We find that the loss factor dramatically increases with applied strain due to the onset of nonlinear dissipation mechanism such as buckling and plasticity. We show that at effective densities around 50% the energy dissipation per cycle in a microlattice outperforms the dissipation in the bulk, giving rise to a "less is more" effect. The present research defines a first step in the application of microlattice materials in vibration absorption.

GRAPHICAL ABSTRACT
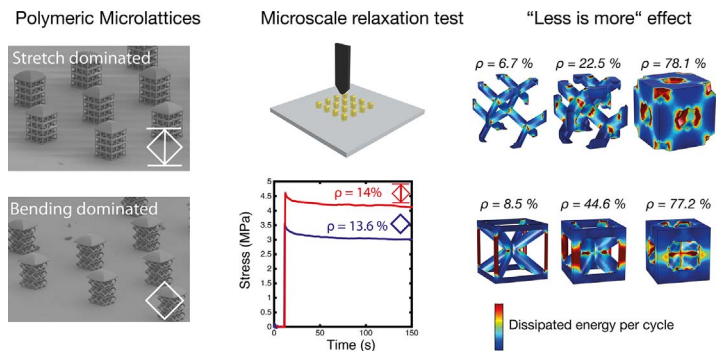
1. I. Introduction

Advances in micro fabrication techniques have led to a paradigm shift in materials design. Instead of using a finite set of available materials, with mechanical properties derived from their atomistic composition, it is now possible to design materials with desired mechanical properties, adjusting the geometry of their microstructure [1–7]. The main technologies to create structured materials with sub-micrometer precision are direct-laser writing, using two-photon poly-merization [8], and interference lithography [9]. These technologies commonly referred to as µ-printing allow for an increasingly large range of applications ranging from optics to biology [10,11]. Special

* Corresponding author.
  E-mail address: daraio@caltech.edu (C. Daraio).

interest lies in the fabrication of microscale materials with advanced mechanical properties [12]. Within this class, microlattice materials consist of micro-and nano-scale truss-like elements that are assembled in three-dimensions. It has been shown that hollow, metallic or ceramic microlattices are strong, yet extremely lightweight [2,3,13]. For nanometer-thin ceramic lattices, size effects also increase the damage tolerance [2]. Besides the possibility of adjusting the mechanical properties by varying the microlattice geometry it is also possible to adjust the base material properties. For instance, the degree of polymerization in polymers offers the ability to adjust the mechanical as well as optical properties [14,15]. Other approaches used to increase the strength and stiffness of microlattices include pyrolysis [5], the use of a metallic base material [16] or the doping of photoresist with nanoparticles [17].

Microlattices have been proposed for a number of applications, ranging from electrodes for batteries [18], photonic crystals for strain sensing [19] and for use as ultrasonic filters exploiting local resonances [20,21]. Microlattices are also promising as energy and sound absorbing materials, for instance in helmets or other protective equipment. Foam materials are traditionally used in these applications, as they can be produced relatively easily and their properties can be adjusted over a wide range [22–25]. Traditional foams can be made from metallic [26,27] or polymeric [28,29] base materials and their mechanical properties are adjusted mainly by changing their effective density. However, due to their randomized architecture the mechanical properties of foams are up to one order of magnitude inferior when compared to highly architected periodic microlattices [30]. Therefore, microlattice materials have a large potential in energy absorption. Some energy dissipating microlattices exploit plastic deformation in the hinges at large strains [31,32], while others use carefully designed instabilities (i.e., buckling of structures) [33,34]. Buckling induces spontaneous bifurcations that, in turn, excite high frequency structural vibrations in the lattices [35]. These vibrations are then damped by viscoelasticity, a dissipation mechanism particularly important for hollow metallic microlattices [36–38]. Lattices that undergo plastic deformation and/ or buckling are primarily designed for impact mitigation. However, they can usually only be used once, as the dissipated energy at each loading cycle decreases dramatically with increasing number of cycles, due to accumulating failure [37]. Differently than impact, vibration absorption problems benefit from continuous energy dissipation over many cycles of mechanical loading. The damping of structural vibrations is important in many engineering systems, including machinery, automotive, aircrafts and satellites. As structural materials typically show a very low amount of intrinsic damping [39], they are often combined with viscoelastic materials, such as foams, to deliver a sufficient amount of vibration mitigation. The viscoelastic dissipation in random foam materials is well documented [28,29], but it remains unexplored in structured microlattices.

Here, we study the viscoelastic properties of polymeric microlattices fabricated using direct-laser writing (DLW) 2-photon lithography. We perform relaxation experiments on two representative microlattices, one bending and one stretch dominated, and study their viscous response. Moreover, we show for the first time how microstructure in microlattice materials impacts their viscoelastic response. We vary their effective density and strain level, to identify the key parameters for design. Results show that tuning the effective density permits to tailor the ratio between stiffness and energy dissipation over a wide range. We inform the experiments with finite element computations, using a generalized Maxwell constitutive model [40]. The computations match the experimental measurements and give insights into the dissipation mechanisms and the precise distribution of mechanical fields in the structures.

## 2. II. Materials and methods

2.1. Lattice design and fabrication

In our work we focus on the control of mechanical properties by adjusting the microstructure, apart from the possibility of controlling their properties by changing the polymer base or degree of polymerization [15].

We design microlattice materials using the CAD environment of Comsol Multiphysics ©. We focus on stretch dominated (SD) (Fig. 1(a)–(c)) and bending dominated (BD) microstructures (Fig. 1(d)–(f)). In SD, the trusses show a high degree of connectivity and some trusses are loaded in stretch/compression, which makes the structural response of the microlattices stiffer [41]. BD structures have a lower degree of connectivity and exhibit an overall more compliant structural response. The unit cells (UC) are completely described by two parameters: the cell size a and the truss diameter r. In the following, we fix the cell size to $a_{SD} = 26\ \mu m$ and $a_{BD} = 33\ \mu m$. We fabricate samples for compression testing by tessellating the UC's, Fig. 1(b), (e). We found $3 \times 3 \times 4$ UC's sufficient to represent the mechanical response of the lattice. The small number of necessary unit cells stems from the uniaxial stress state.

For fabrication, we use a commercially available DLW tool based on 2-photon polymerization (Nanoscribe™). The CAD designed structures are exported as .stl files and Describe© is used for further processing. In Describe the 3D structures are discretized in vertical slices of 0.5 μm thickness. Each slice is then hatched into lines with a distance of 0.35 μm that form the input to the direct laser-writing tool. The x-y plane resolution of the tool is higher than the resolution in z due to the elliptical voxel cross section. The fabrication process can be divided into 4 main steps: (i) Sample preparation step: ITO coated glass substrates are cleaned with acetone and isopropanol in a sonicator and liquid photoresist (IP-Dip™) is drop casted onto the substrates. (ii) Writing step: samples are fabricated in dip-in immersion process, where the $25 \times$ (Zeiss, LCI Plan Neofluar, NA = 0.8) microscope objective is in direct contact with the liquid photoresist. We use the galvo-scanning mode with a laser power of 40 mW reaching the objective after an acousto-optic modulator and a scan speed of 25,000 μm/s. (iii) Cleaning and drying step: samples are developed for 10 min in OrmoDev600™ prior to 5 min in isopropanol washing. Afterwards the structures are left to dry in air. (iv) Baking step: before mechanical testing, structures undergo a post baking treatment (as described in [42]) to increase their mechanical stability and fully cure the resist. Samples are heated up in an oven (Thermo Fischer Scientific) from room temperature to 200 ˚C, with a heating rate < 10 ˚C/min, followed by a 15 min hold and a final cooling under a small rate (< 10 ˚C/min) to room temperature.

The samples (Fig. 1(b), (e)) have an overall height of approximately 100 μm and a side length of 70 μm. On top of the lattice samples, we fabricate a rounded plate, which permits to apply a homogeneous compression to the samples. Note that the writing process produces non-smooth surfaces of the truss elements (see Fig. 1(c), (f)), which will not be considered in the following analysis. However, the small irregularities are defects, which have a clear role for the onset of buckling or fatigue in the truss elements. The amplitude of the wrinkles is approximately 0.1 μm with a wavelength of 0.35 μm. Another aspect of the writing process is the residual deformation due to residual stresses, which can be observed by slightly curved vertical edges of the microlattice structures. This aspect will equally be neglected in the analysis.

One of the main parameters determining the mechanical behavior of a cellular material is its effective density [25,32]. To study the influence of varying effective density, $\rho_e = \frac{\rho_L}{\rho} = \frac{V_L}{V}$, where the index L describes the density/volume of the microlattice, we vary the radius of the constituting truss elements between 1 and 5.5 μm (Fig. 2(a), (b)). For a
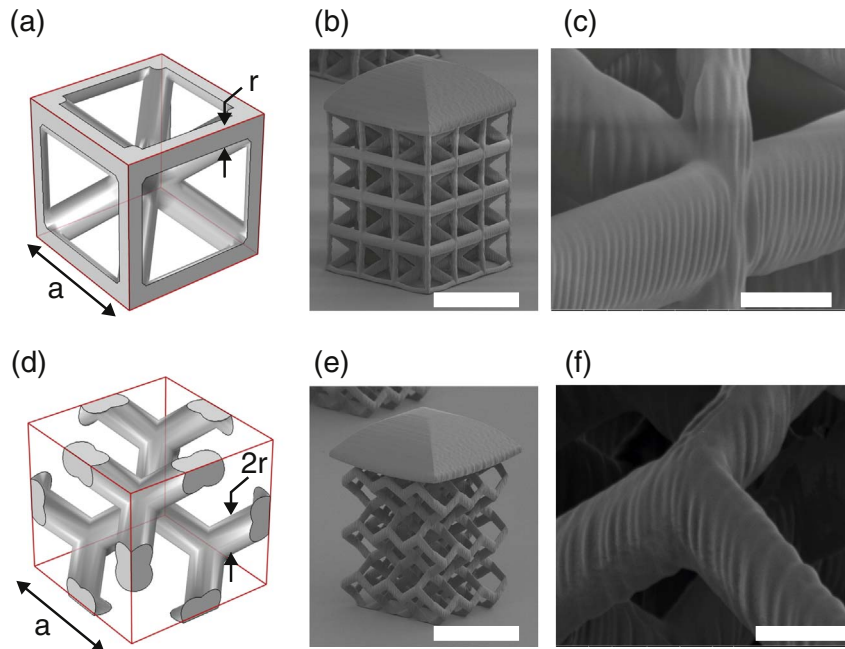
Fig. 1. Unit cell geometries. (a) Stretch dominated cubic unit-cell with lattice constant a and truss radius r. (b) SEM micrograph of stretch dominated compression-test sample, scale bar is 50 μm. (c) Close-up of stretch dominated sample, scale bar is 10 μm. (d) Bending dominated cubic unit-cell with lattice constant a and truss radius r. (e) SEM micrograph of bending dominated compression-test sample, scale bar is 50 μm. (f) Close-up of bending dominated sample, scale bar is 10 μm.

lattice fabricated with a single material, the effective density is equivalent to the volume-filling fraction, $\frac{V_L}{V}$, between solid material and the overall volume of the cubic UC. Effective densities are calculated based on the CAD models that have been informed by SEM images. The chosen truss radii result in effective densities between 8% and 65% for stretch dominated structures and 4% and 45% for bending dominated structures respectively (see Fig. 2(a), (b)). The resulting effective densities of the SD structures are larger at equal radius due to the higher number of trusses per unit cell and the higher connectivity of trusses. In general, the minimum radius is restricted by structural stability, while the maximum radius is set close to the merging of individual trusses.

2.2. Micro scale relaxation experiments and generalized Maxwell model

For our experiments, we use a customized compression test setup based on the commercial FemtoTools™ setup (Fig. 3(a)). We perform displacement-controlled tests, by adjusting the x,y,z position of the capacitive force sensor and measuring the resulting force. To automate our relaxation tests, we program a custom LabView interface. In our experiments, we used two different sensors (FTS10000, FTS100000, with a maximum force of 10.000 μN and 100.000 μN) depending on the required force range. These two sensors have a flat tip area of 50 × 50 μm, which allows compatibility with the compression samples (Fig. 1(b), (e)). Two perpendicular microscopes are used to monitor the sensor position relative to the samples. The force sensors have a finite stiffness when compared to typical sample
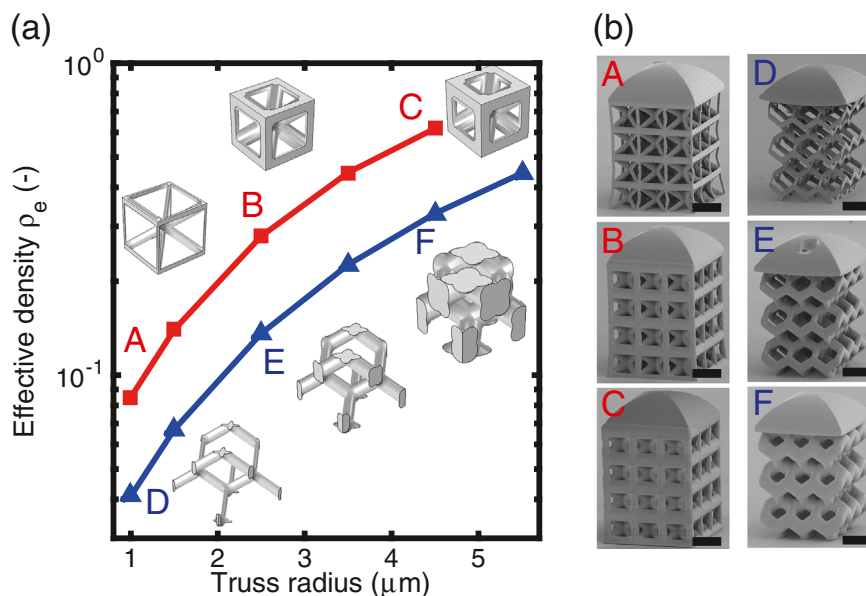
Fig. 2. Varying unit cell densities. (a) Effective lattice densities as a function of truss radius r for SD (red) and BD (blue) structures. (b) Panels A-F showing SEM micrographs of fabricated micro-compression samples with varying truss radius, scale bar is 25 μm. (For interpretation of the references to color in this figure legend, the reader is referred to the web version of this article.)
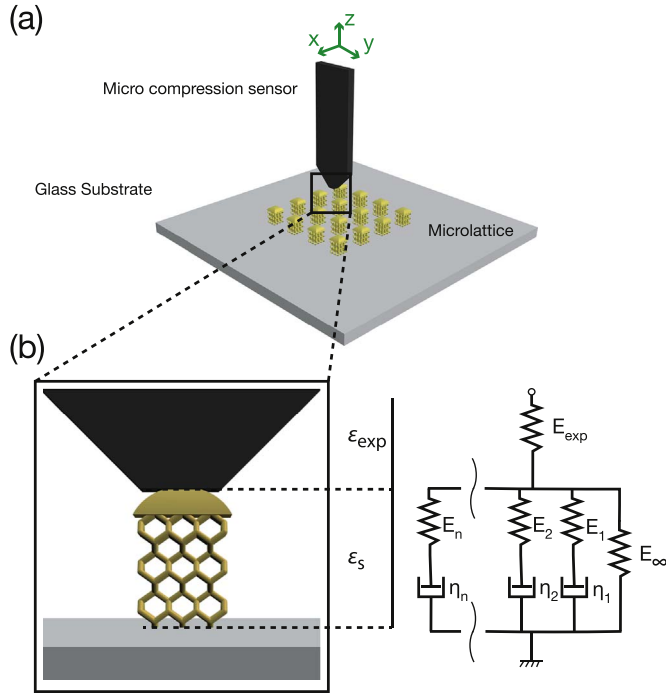
Fig. 3. Experimental setup and Maxwell model. (a) Schematic of the experimental setup. (b) Testing setup for one microlattice sample and the corresponding rheological model.

stiffness in our experiment. Therefore, there is a non-negligible displacement in the force sensors for the performed experiments. The total measured displacement u is due to the deformation in the sensor spring u_{exp} and the displacement in the sample u_s. The actual displacement in the sample u_s can be written as:

$$u_s = u - u_{exp} = u - \frac{F}{K_{exp}} \quad ,$$

(1)

The sensor stiffness is assumed to be non-viscous and can be obtained by measuring directly on the stiff glass substrate.

Relaxation experiments are performed by bringing the sensor in close proximity to the sample and imposing a constant displacement for a prescribed amount of time (typically 400 s) (Fig. 3(b)). In the following, we consider the effective stress and strain of the lattice structure, $\sigma = \frac{F}{A_L}$ and $\varepsilon_S = \frac{u_S}{H_L}$, respectively. Here A_L denotes the projected area of the lattice and H_L the lattice height. Note that these are effective properties and should not be mistaken with the microscopic stress $\hat{\sigma}$ and strain $\hat{\varepsilon}$ that occur at the individual trusses. The goal

of the relaxation experiments is to obtain the time dependent relaxation modulus of the analyzed sample:

$$E(t) = \frac{\sigma(t)}{\varepsilon(t)}$$

(2)

The performed relaxation test deviates slightly from an ideal relaxation experiment: (i) The loading rate is finite (around $1\ \text{s}^{-1}$), and (ii) the applied strain is not constant throughout the experiment (for a given relaxing force the displacement in the sample increases, see Eq. (1)). In linear viscoelasticity, the response to an arbitrary strain history can be predicted by means of the Boltzmann superposition principle [43]:

$$\sigma(t) = \int_{-\infty}^{t} E(t-\tau)\dot{\varepsilon}\ d\tau = \int_{\varepsilon(-\infty)}^{\varepsilon(t)} E(t-\tau)d\varepsilon.$$

(3)

To obtain the relaxation modulus from our experiments, we can discretize this relation. Suppose that we record the strain ε from time $t = 0$ till $t = n\ \Delta t$. Using a time stepping of Δt we can write the stress at $t = m\ \Delta t$:

$$\sigma(m\ \Delta t) = \sum_{i=1}^{m} E(i\ \Delta t)\Delta\varepsilon(i\ \Delta t)$$

(4)

with the incremental strain being $\Delta\varepsilon = \varepsilon(i\ \Delta t) - \varepsilon((i-1)\Delta t)$. We can rewrite this expression in terms of the relaxation modulus at $t = m\ \Delta t$:

$$E(m\ \Delta t) = \frac{\sigma(m\ \Delta t) - \sum_{i=1}^{m-1} E(i\ \Delta t)\Delta\varepsilon(i\ \Delta t)}{\Delta\varepsilon(m\ \Delta t)} \quad .$$

(5)

In our experiments, we use a time stepping of 1 ms.

To gain insights into the viscoelastic behavior, we also model the samples using a generalized Maxwell model (GMM), see Fig. 3(b). This GMM is also used as an input for the material in our FEM simulations. The branches of the model yield relaxation modulus in the form of a discrete Prony series:

$$E(t) = E_\infty + \sum_{i=1}^{n} E_i\ e^{-\frac{t}{\tau_i}} \quad ,$$

(6)

where E_∞ is the relaxed modulus, E_i are the moduli of the different branches and τ_i the corresponding time constants. Note that the GMM is in series with the experimental stiffness E_{exp}. By transforming into the frequency domain, we can obtain the frequency dependent form of the storage and loss modulus.

$$E'(\omega) = E_\infty + \sum_{i=1}^{n} \frac{E_i\omega^2\tau_i^2}{1 + \omega^2\tau_i^2} \quad E''(\omega) = \sum_{i=1}^{n} \frac{E_i\omega\tau_i}{1 + \omega^2\tau_i^2}$$
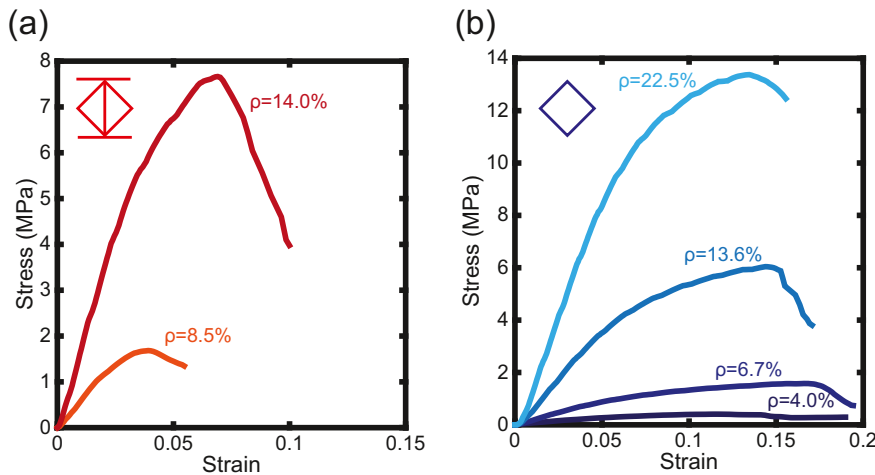
(7)

Fig. 4. Quasi static compression experiments. Quasi static compression curves for SD (a) and BD (b) structures with varying densities.

The loss factor is defined as the ratio between loss and storage modulus: $\eta = \frac{E''}{E'}$. For fitting the GMM to a continuous relaxation spectrum from experimental data, we fix the number of branches to 4 and set the relaxation times manually to avoid the ill-posed optimization problem [40]. A complete analysis over a larger spectrum of temperatures and relaxation times would probably impose the use of a larger number of branches. We use the *lsqcurvefit* function of Matlab© to fit the 5 missing moduli to the experimental curves.

2.3. Finite element modeling

The experiments and the calculation of the effective viscoelastic properties of the microlattices have been complemented with detailed time-domain and frequency-domain analysis, using the finite element package Comsol Multiphysics©. We study only the unit cells of the lattices, with applied periodic boundary conditions on the side faces. The bottom surfaces were fixed and we applied either step (relaxation experiment) or harmonic displacement (frequency domain) on the top surface. The frequency domain simulations are performed to study the dissipated energy per cycle in the different lattices. The meshes were based on the sample's geometry as measured in a scanning electron microscope and contained typically 50×10^3 terahedral elements with approximately 1×10^6 degrees of freedom. The mesh size was verified on quasi-static simulations. Refinement stopped once the final results changed $< 1\%$. The constitutive linear viscoelastic material was a Prony series with 4 branches, equivalent to the GMM described in the preceding section. Inertial effects can be neglected, as the considered time scales are far larger than time scales corresponding to eigenfrequencies of the structures.

3. III. Results

3.1. Static compression experiments

We perform quasi-static measurements at a strain rate of $10^{-3}\,\mathrm{s}^{-1}$ for 6 different structures: SD lattices with a radius of 1 μm and 1.5 μm (Fig. 4(a)) and BD lattices with a radius of 1 μm, 1.5 μm, 2.5 μm and

(a)

(b)

Fig. 5. Failure analysis. Failure modes after a single compression cycle in (a) SD structures with and effective density of 8.5% and (b) BD structures with an effective density of 13.6%. Scale bar in overview is 25 μm and in close-up is 10 μm.

3.5 μm (Fig. 4(b)).

The measurements show the complete loading range, which begins with an initially linear region, followed by a softening region, characterized by buckling of the beam elements, and failure, which occurs at the nodes. The onset of failure at the nodes is responsible for the load reduction (Fig. 4(a), (b)). SD structures with an initial static stiffness of 172.2 MPa reach a maximum strength of 7.65 MPa, while the same geometry with an initial stiffness of 60.4 MPa reach a maximum strength of 1.68 MPa. The linear range of SD structures is typically up to 2–3% of the effective strain. For BD structures, we observe absolute strengths values increasing from 0.41 MPa, 1.58 MPa, 6.03 MPa to 13.38 MPa, when the static stiffness increases from 5.43 MPa, 19.78 MPa, 77.26 MPa to 180.16 MPa. The linear elastic region is slightly larger for the bending dominated structures, up to 6% of the effective strain. At similar densities (e.g., 14.0% for SD and 13.6% for BD) the stiffness of the SD lattice is also significantly higher than that of the BD lattice. The increased stiffness in the SD lattices arises from the higher connectivity of the members and their tensile response during deformation. We also analyzed the tested samples for visual signs of damage after full compression (Fig. 5(a), (b)).

The stretch dominated lattices showed primarily failure induced by the buckling of the vertically aligned truss elements, which are loaded in compression (Fig. 5(a)). For the $r_0 = 1.5\,\mu m$ SD structure we estimated the first buckling failure mode at $\approx 6\%$ strain based on linear buckling finite element analysis of the full sample. The vertical bars are thinner than the horizontal bars due to the elongated voxel geometry, possibly limiting the mechanical performance of SD structures. On the contrary, BD lattices fail mainly at the nodes, where the highest stress concentrations occur, induced by bending (Fig. 5(b)), before the onset of buckling. Despite the several through cracks observed by visual inspection under the SEM, the samples show a high degree of long-term recovery, up to 90%, after one full loading cycle. This recovery could eventually be enhanced using thermal annealing and further investigations are needed to assess the complete role of temperature and/or curing on damaged structures after loading.

3.2. Lattice relaxation experiment

Relaxation experiments were performed at strains 2% and 4% for SD and 4% and 8% for BD structures. The large strains (4%, 8%, respectively) allow studying the influence of the onset of buckling and plasticity on the viscoelastic dissipation. Additionally, the strain for BD lattices is set to an overall higher value, as the linear elastic range of these structures observed in quasi-static experiments is larger (Fig. 4(b)). Typical measurement curves for two different structures show that the relaxation test deviates from the ideal case (Fig. 6(a)). During measurements, the strain in the sample increases slightly due to relaxing stress that reduced the displacement in the sensor (Eq. (1)). A clear relaxation in stress in the observed time frame is visible (Fig. 6(b)). After approximately 200 s, we observe a plateau of the effective stress. For each measured sample, we can calculate the experimental relaxation modulus (Fig. 6(c)) from Eq. (5). We test at least 3 samples for each parameterization and found a low variability between samples (< 5%), highlighting the reproducibility of the fabrication technique. Additionally, we use a GMM with 4 branches to fit to the average relaxation modulus of each structure (Fig. 6(c)). We found 4 times constants at 0.1 s, 1 s, 10 s and 50 s sufficient to obtain a good fit to all the experimental measurements (error < 5%). Using Eqs. (6) and (7), we can calculate the frequency dependent loss and storage moduli on the basis of the GMM (Fig. 6(d)). The multiple variations in the shape of E' and E'' observed in Fig. 6(d) can generally be associated with a more complex distribution of polymeric chains in the network.

The results of the relaxation experiments are summarized in Table I. The loss factors of both the SD and BD structures are very similar at small strains.

To gain insights into the influence of elevated strains, we perform relaxation tests at 8% for BD and 4% for SD. These strains are outside
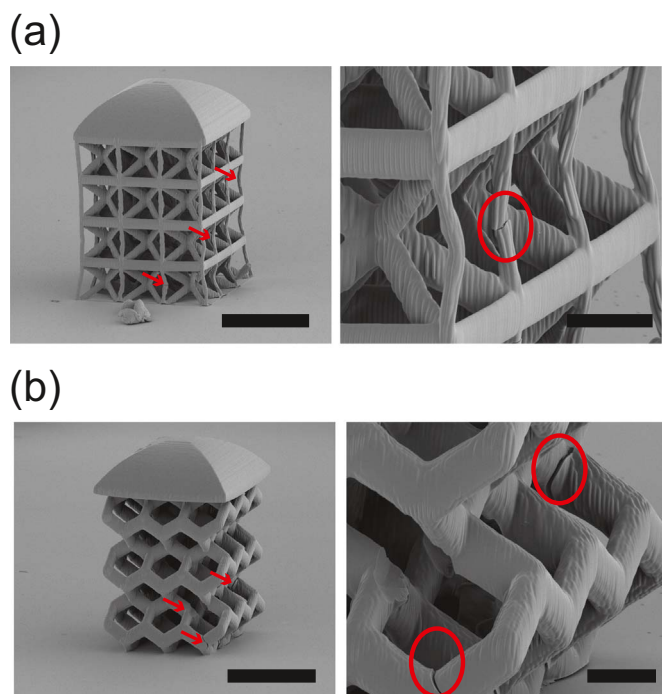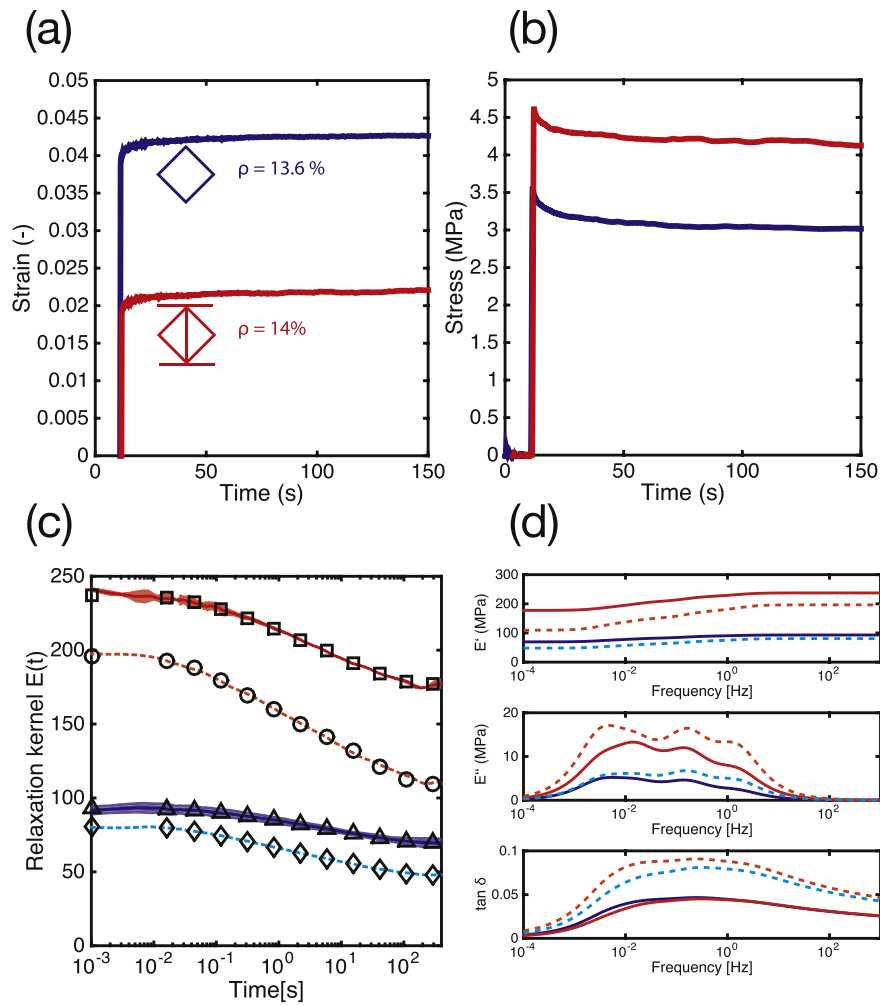
Fig. 6. Small scale relaxation experiments. (a) Strain history in the sample for typical relaxation experiment of SD (red) and BD (blue) structures. (b) Measured stress-relaxation for BD and SD structures. (c) Calculated relaxation modulus for BD and SD structures. The shaded area shows the standard deviation for BD (blue, solid) and SD (red, solid). Dashed lines represent experiments performed at twice the initial strain. Markers represent GMM fits using 4 branches. (d) Storage modulus (E'), loss-modulus (E''), and loss-factor calculated from the GMM in (c). (For interpretation of the references to color in this figure legend, the reader is referred to the web version of this article.)

the linear elastic region (Fig. 4(a), (b)) and are expected to trigger other dissipation channels. We observe two distinct effects: (i) Both the relaxed and unrelaxed moduli are reduced, which is coherent with the reduced slope in the nonlinear stress-strain relation (Fig. 4(a), (b)); and (ii) the difference between unrelaxed and relaxed modulus increases. This difference is related to the increasing dissipation, which reflects also in the increase loss factor for larger strain (Fig. 6(d) and Table I). The increase in loss-factor is approximately two-fold for the large strain experiments, from 0.044 to 0.091 for SD structures. The maximum loss factor in our experiments occurs at relatively low frequencies of 0.27 Hz. For small strains, we find that the measured loss factor is

consistent with loss factors of typical acrylic polymers [44]. However, for large strains, the reached losses dramatically increase as observed also in conventional foam materials [29].

3.3. Density scaling laws

The properties of conventional foams are typically described in the form of density scaling laws [41]. For an ideal, bending dominated foam/lattice the static stiffness scales $E \propto \rho^2$. We find a consistent scaling for the bending dominated lattices in our experiments (Fig. 7(a)). Interestingly, the stretch dominated lattices in our experiments (in the

Table I
Results of micro-scale relaxation experiments. Results for initial, relaxed modulus are mean values from at least 3 measurements with an error of < 5%.

Lattice type	Strain ε_0 (%)	Radius r_0 (μm)	Effective density (%)	Initial modulus E_0 (MPa)	Relaxed modulus E_∞ (MPa)	Loss factor η (−)	Damping FOM ψ (−)
SD	2	1.0	8.5	63.1	50.1	0.035	1.52
SD	2	1.5	14.0	234.3	176.1	0.044	1.76
SD	4	1.5	14.0	196.2	109.6	0.091	3.11
BD	4	1.0	4.1	6.9	5.4	0.038	1.63
BD	4	1.5	6.7	22.8	17.8	0.040	1.56
BD	4	2.5	13.6	94.4	69.5	0.052	1.57
BD	4	3.5	22.6	215.4	164.3	0.052	1.20
BD	8	2.5	13.6	80.6	48.07	0.081	2.17
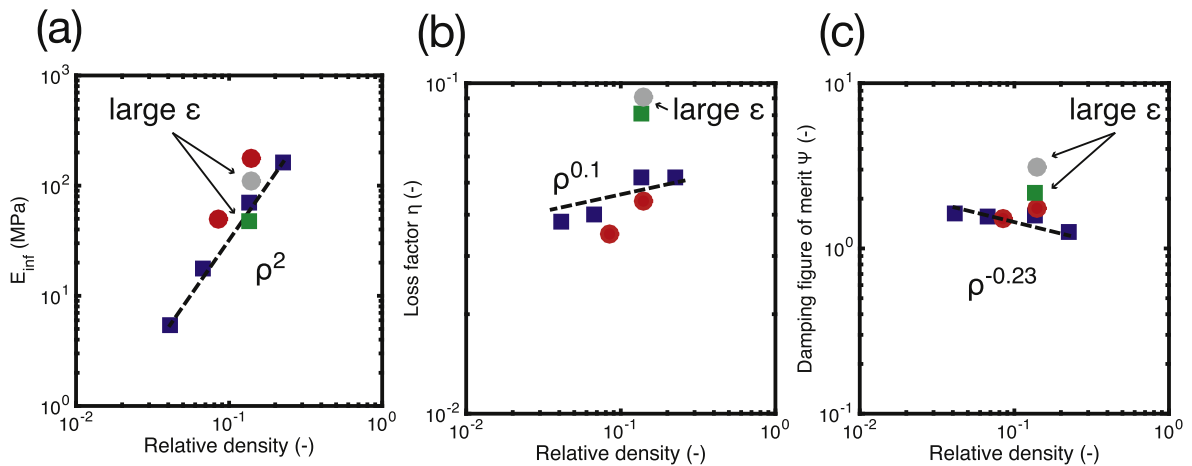
Fig. 7. Scaling laws. (a) Scaling of the relaxed Young's modulus as a function of relative density for BD (blue, square) and SD (red, dot). Experiments at large density are shown for BD (green, square) and SD (grey, dot). (b) Scaling of the loss factor as a function of relative density for BD (blue, square) and SD (red, dot). Experiments at large density are shown for BD (green, square) and SD (grey, dot). (c) Scaling of the damping figure of merit as a function of relative density for BD (blue, square) and SD (red, dot). Experiments at large density are shown for BD (green, square) and SD (grey, dot). (For interpretation of the references to color in this figure legend, the reader is referred to the web version of this article.)

two tested configurations) also present a quadratic scaling with density, departing from the theoretical linear scaling predicted for stretch dominated lattices. We attribute this effect to the non-perfect geometry of the fabricated microlattices (see Figs. 1,2). For example, some of the vertical trusses seem to buckle easily, possibly degrading the overall lattice performance at lower densities. We also analyzed the scaling of the loss factor (η, from the GMM fit) with the effective density of the different lattice structures (Fig. 7(b)). In BD structures, we observe a weak scaling ($\eta \propto \rho^{0.1}$), possibly related to nonlinear effects, such as plasticity at the nodes. These findings imply that for BD structures it is possible to largely vary the Young's modulus (by a factor of 30), by changing the effective density of the lattices, while the loss factor changes only by 30%.

We also investigate the damping figure of merit (ψ) of the tested materials (Fig. 7(c)):

$$\psi = \frac{E^{\frac{1}{3}} \eta}{\rho} \tag{8}$$

This non-dimensional number is a measure of how fast a sandwich

plate, subjected to forced vibrations, would come to rest after the forcing is removed [37,45]. The damping figure of merit decreases with density. The observed values for ψ vary between 1.20 and 3.11, significantly higher than the values observed in hollow lattice materials [37]. This increased ψ is related to a more dissipative base material as compared to metallic or ceramic lattices. These results suggest that, especially for vibration problems, polymeric microlattices can be superior to hollow microlattices. This increased damping capabilities, however, come at the cost of a larger effective density.

3.4. Time domain finite element simulations

We perform time domain finite elements simulations on the BD and SD lattice structures. For these simulations, we analyze the deformation in a single UC (Fig. 8(a)). We fix the lower faces of the unit cell and apply a step displacement resulting in 4% strain. On the side faces of the UC, we apply periodic boundary conditions to avoid boundary effects. The resulting stress can be obtained by integration of the local stress in the z-direction, on the top surface Ω:
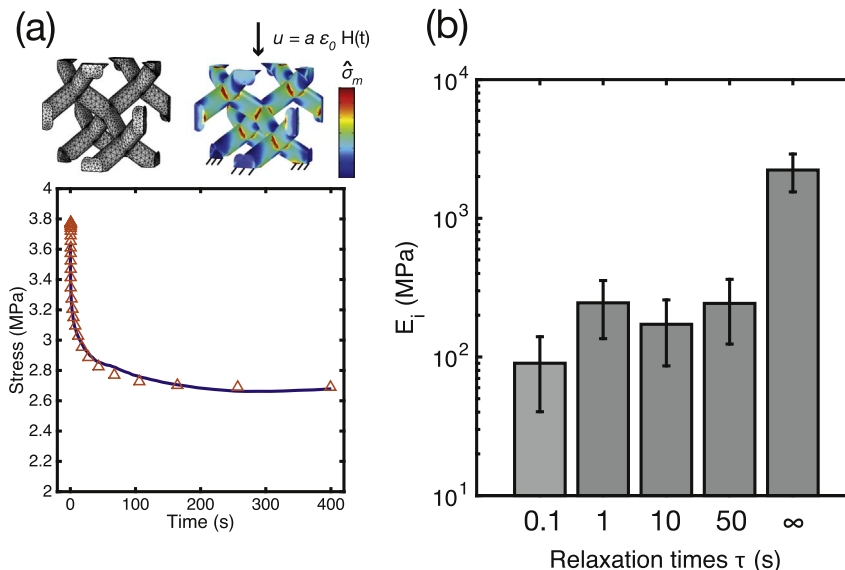
Fig. 8. Time domain simulations FEM. (a) Time domain simulation of BD structures. The solid line represents the experimental data and the triangular markers the simulation results. The insets show the FEM mesh (left) and the von Mises stress distribution (right). (b) Calculation of the individual branch moduli for the generalized Maxwell model, as a function of different relaxation times. The error bars stem from the variance of experiments using all samples as reported in Table I.
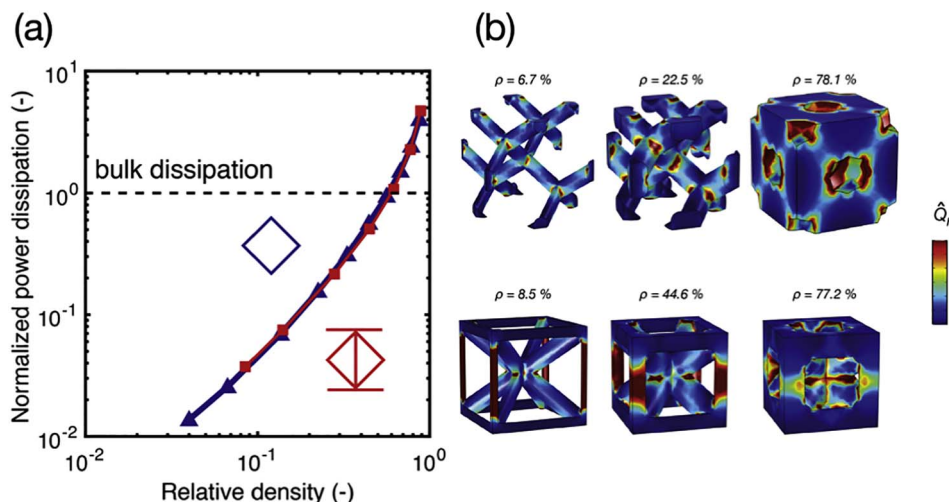
Fig. 9. Frequency domain simulation. (a) Power dissipation per cycle as a function of relative density for the two lattice geometries considered: BD (blue) and SD (red). (b) Von Mises stress distribution for varying densities of BD (top row), SD (bottom row) structures. (For interpretation of the references to color in this figure legend, the reader is referred to the web version of this article.)

$$\sigma(t) = \frac{1}{a^2} \int_\Omega \hat{\sigma}_z(t) dA \tag{9}$$

From the stress, we can obtain the relaxation module from Eq. (2). To find the base material properties, we exploit the linear relation $E_L(t) = C \times E(t)$ between the relaxation modulus of the base material $E(t)$ and the effective relaxation modulus of the lattice $E_L(t)$, with a linear constant, C, that is valid in linear viscoelasticity [29,46]. We use the branches obtained from experimental data (Eq. (6)) as an input to the viscoelastic properties in Comsol Multiphysics. We assume a constant Poisson's ratio of $\nu = 0.49$. In Comsol the viscoelastic branches are expressed in terms of shear moduli, which are related to the experimentally measured Young's moduli by:

$$G_i = \frac{E_i}{2(1 + \nu)} \tag{10}$$

We perform one simulation with the experimental branches of the GMM and then find the linear factor C that is necessary to obtain the same instantaneous modulus (see Fig. 8(a)). This approach allows to extract the base material viscoelastic properties from the relaxation experiments. This numerical procedure results in an excellent fit to the experimental data (Fig. 8(a)). We also find a good agreement between the occurrence of the maximum von Mises stress in BD structures (Fig. 8(a)) and the observed plastic failure modes in the joints (Fig. 5(b)). Undergoing this procedure for all experimental lattices allows predicting the viscoelastic base material properties within in a narrow range (Fig. 8(b)). We find $E_\infty = 2.22 \pm 0.67$ GPa for the relaxed modulus of the photoresist IP-Dip™, used in the lattices fabrication. The predicted relaxed modulus agrees also well with previous works [42,47,48]. The linear factor C can be also used to extrapolate the microlattice viscoelastic properties if the base material is changed.

3.5. Frequency domain finite elements

To study lattice geometries that couldn't be studied in our experimental campaign, we employ frequency domain finite element simulations of BD and SD structures. Here, we subject the same UC as in the time domain simulation to a harmonic excitation with the strain ε_0. As a measure of performance, we identify the dissipated energy per cycle Q_h in one UC, which is related to the loss factor η and the maximum stored elastic energy W_h:

$$Q_h = 2\pi \eta W_h \tag{11}$$

From the GMM for the base material (Fig. 8(b)), we find that 0.27 Hz

corresponds to the frequency with the maximum loss factor, which is used as harmonic frequency in all simulations. We study the overall dissipated energy per cycle in one unit cell, normalized by the energy dissipated in a solid block of the same polymer. Interestingly, we find that for effective densities of approximately 50% the energy dissipated in a microlattice is significantly larger than the energy dissipated in a bulk cube of the same size (Fig. 9(a)). This can be accounted to effects of local stress concentrations that increase the hysteresis locally. These results are have not been experimentally validated due to a limit in force range that prevents the testing of high density (stiff) structures. Additionally, in the numerical results we observe a variation in the dissipated energy distribution of the lattice, once the density is increased (Fig. 9(b)). This can also be explained by variations in the stress concentration: at lower density, local stress concentrations around the nodes of the lattice dominate the response. However, for increasing density, the dissipation becomes more uniformly distributed in the lattice. For very large beam radii (i.e., large densities), the beam elements start to merge, significantly altering the original lattice geometry and evolving towards porous material. In this case, as expected, the dissipation is distributed around the free surfaces and there is a large amount of shear. For SD structures at low densities, most of the dissipated energy is concentrated near the nodes in the vertical trusses. For larger densities, as energy concentration decreases with increasing volume or density the dissipation is more evenly spread across the UC. This difference in both spatial distribution and quantitative values will lead to different damage and failure mechanism, which have not been studied here.

4. IV. Conclusion

In summary, we have fabricated and analyzed the linear viscoelastic properties of polymeric microlattice materials. This analysis is an important step from previous works that were mainly addressing the quasi static, i.e. elastic or elasto-plastic, properties of microlattices. We developed a versatile experimental procedure to study stress relaxation in microlattices, for time scales up to 400 s. Our experimental study revealed that the effective Young's modulus of polymeric lattice structures, with different lattice topologies, can be adjusted by adapting their effective lattice densities. We found that, in the considered density range, the loss factor is only slightly scaling with the lattice density. We also studied the loss factor at elevated strains and found an increased loss factor and damping figure of merit of up to 3.1. The results show that the loss factor of microlattice materials is mainly increased by large strains, which is important for impact mitigation. In structural vibration absorption applications, the reached strains can be quite small. In these problems, the use of a more dissipative base material or composite is

beneficial to increase the damping capabilities. Numerical simulations show that high effective density lattices outperform bulk polymeric blocks in energy dissipation. This result is counter-intuitive, as it predicts an increased dissipation with using effectively less material. To increase the range of covered frequencies, experiments at varying temperatures could be performed, exploiting the temperature/frequency equivalence of polymer viscoelasticity.

Acknowledgements

References

[1] T.A. Schaedler, A.J. Jacobsen, A. Torrents, A.E. Sorensen, J. Lian, J.R. Greer, L. Valdevit, W.B. Carter, Ultralight metallic microlattices, Science 334 (2011) 962–965, http://dx.doi.org/10.1126/science.1211649.

[2] D. Jang, L.R. Meza, F. Greer, J.R. Greer, Fabrication and deformation of three-dimensional hollow ceramic nanostructures, Nat. Mater. 12 (2013) 893–898, http://dx.doi.org/10.1038/nmat3738.

[3] L.R. Meza, S. Das, J.R. Greer, Strong, Lightweight and Recoverable Three - Dimensional Ceramic Nanolattices, Science 345 (2014) 1322–1326 (80), http://dx.doi.org/10.1126/science.1255908.

[4] J. Bauer, S. Hengsbach, I. Tesari, R. Schwaiger, O. Kraft, High-strength cellular ceramic composites with 3D microarchitecture, Proc. Natl. Acad. Sci. 111 (2014) 2453–2458 http://www.pnas.org/content/early/2014/01/29/1315147111.abstract.

[5] J. Bauer, A. Schroer, R. Schwaiger, O. Kraft, Approaching theoretical strength in glassy carbon nanolattices, Nat. Mater. 8 (2016), http://dx.doi.org/10.1038/nmat4561.

[6] M. Mieszala, M. Hasegawa, G. Guillonneau, J. Bauer, R. Raghavan, C. Frantz, O. Kraft, S. Mischler, J. Michler, L. Philippe, Micromechanics of Amorphous Metal/Polymer Hybrid Structures with 3D Cellular Architectures: Size Effects, Buckling Behavior, and Energy Absorption Capability, (2017), pp. 1–13, http://dx.doi.org/10.1002/smll.201602514.

[7] X. Zheng, H. Lee, T.H. Weisgraber, M. Shusteff, J. Den Otte, E.B. Duoss, J.D. Kuntz, M.M. Biener, Q. Ge, J.A. Jackson, S.O. Kucheyev, N.X. Fang, C.M. Spadaccini, Ultralight, ultrastiff mechanical metamaterials, Science 344 (2014) 1373–1377, http://dx.doi.org/10.1126/science.1252291.

[8] M. Deubel, G. von Freymann, M. Wegener, S. Pereira, K. Busch, C.M. Soukoulis, Direct laser writing of three-dimensional photonic-crystal templates for telecommunications, Nat. Mater. 3 (2004) 444–447, http://dx.doi.org/10.1038/nmat1155.

[9] J.H. Jang, C.K. Ullal, M. Maldovan, T. Gorishnyy, S. Kooi, C.Y. Koh, E.L. Thomas, 3D micro- and nanostructures via interference lithography, Adv. Funct. Mater. 17 (2007) 3027–3041, http://dx.doi.org/10.1002/adfm.200700140.

[10] J.K. Hohmann, M. Renner, E.H. Waller, G. von Freymann, Three-dimensional mu-printing: an enabling technology, Adv. Opt. Mater. 3 (2015) 1488–1507, http://dx.doi.org/10.1002/adom.201500328.

[11] M. Malinauskas, A. Žukauskas, S. Hasegawa, Y. Hayasaki, V. Mizeikis, R. Buividas, S. Juodkazis, Ultrafast laser processing of materials: from science to industry, Light Sci. Appl. 5 (2016) e16133, , http://dx.doi.org/10.1038/lsa.2016.133.

[12] J.H. Lee, J.P. Singer, E.L. Thomas, Micro-/nanostructured mechanical metamaterials, Adv. Mater. 24 (2012) 4782–4810, http://dx.doi.org/10.1002/adma.201201644.

[13] J. Rys, L. Valdevit, T.A. Schaedler, A.J. Jacobsen, W.B. Carter, J.R. Greer, Fabrication and deformation of metallic glass micro-lattices, Adv. Eng. Mater. 16 (2014) 889–896, http://dx.doi.org/10.1002/adem.201300454.

[14] L.J. Jiang, Y.S. Zhou, W. Xiong, Y. Gao, X. Huang, L. Jiang, T. Baldacchini, J.-F. Silvain, Y.F. Lu, Two-photon polymerization: investigation of chemical and mechanical properties of resins using Raman microspectroscopy, Opt. Lett. 39 (2014) 3034–3037, http://dx.doi.org/10.1364/OL.39.003034.

[15] A. Zukauskas, I. Matulaitiene, D. Paipulas, G. Niaura, M. Malinauskas, R. Gadonas, Tuning the refractive index in 3D direct laser writing lithography: towards GRIN microoptics, Laser Photonics Rev. 9 (2015) 706–712, http://dx.doi.org/10.1002/lpor.201500170.

[16] X. Wendy Gu, J.R. Greer, Ultra-strong architected Cu meso-lattices, Extrem. Mech. Lett. 2 (2015) 7–14, http://dx.doi.org/10.1016/j.eml.2015.01.006.

[17] W. Xiong, Y. Liu, L.J. Jiang, Y.S. Zhou, D.W. Li, L. Jiang, J.F. Silvain, Y.F. Lu, Laser-directed assembly of aligned carbon nanotubes in three dimensions for multi-functional device fabrication, Adv. Mater. 28 (2016) 2002–2009, http://dx.doi.org/10.1002/adma.201505516.

[18] C. Xu, B.M. Gallant, P.U. Wunderlich, T. Lohmann, J.R. Greer, Three-dimensional Au microlattices as positive electrodes for Li-O$_2$ batteries, ACS Nano 9 (2015) 5876–5883, http://dx.doi.org/10.1021/acsnano.5b00443.

[19] V.F. Chernov, H. Alaeian, J.A. Dionne, J.R. Greer, Polymer lattices as mechanically tunable 3-dimensional photonic crystals operating in the infrared, Appl. Phys. Lett. 107 (2015) 101905, http://dx.doi.org/10.1063/1.4930819.

[20] S. Krödel, T. Delpero, A. Bergamini, P. Ermanni, D.M. Kochmann, 3D auxetic microlattices with independently controllable acoustic band gaps and quasi-static elastic moduli, Adv. Eng. Mater. 16 (2013) 357–363, http://dx.doi.org/10.1002/adem.201300264.

[21] S. Krödel, C. Daraio, Microlattice metamaterials for tailoring ultrasonic transmission with elastoacoustic hybridization, Phys. Rev. Appl. 6 (2016) 64005, http://dx.doi.org/10.1103/PhysRevApplied.6.064005.

[22] L.J. Gibson, M.F. Ashby, Cellular Solids: Structure and Properties, (1990), http://dx.doi.org/10.2277/0521499119.

[23] P. Göransson, Acoustic and vibrational damping in porous solids, Phil. Trans. R. Soc. A 364 (2006) 89–108, http://dx.doi.org/10.1098/rsta.2005.1688.

[24] N.A. Fleck, V.S. Deshpande, M.F. Ashby, Micro-architectured materials: past, present and future, Philos. Transact. A Math. Phys. Eng. Sci. 466 (2010) 2495–2516, http://dx.doi.org/10.1098/rspa.2010.0215.

[25] M.F. Ashby, The properties of foams and lattices, Philos. Trans. R. Soc. A Math. Phys. Eng. Sci. 364 (2006) 15–30, http://dx.doi.org/10.1098/rsta.2005.1678.

[26] W.Y. Jang, S. Kyriakides, On the crushing of aluminum open-cell foams: Part I. Experiments, Int. J. Solids Struct. 46 (2009) 617–634, http://dx.doi.org/10.1016/j.ijsolstr.2008.09.008.

[27] W.Y. Jang, S. Kyriakides, On the crushing of aluminum open-cell foams: part II analysis, Int. J. Solids Struct. 46 (2009) 635–650, http://dx.doi.org/10.1016/j.ijsolstr.2008.10.016.

[28] F. Saint-Michel, L. Chazeau, J.-Y. Cavaillé, E. Chabert, Mechanical properties of high density polyurethane foams: I. Effect of the density, Compos. Sci. Technol. 66 (2006) 2700–2708, http://dx.doi.org/10.1016/j.compscitech.2006.03.009.

[29] H.X. Zhu, N.J. Mills, Modelling the creep of open-cell polymer foams, J. Mech. Phys. Solids 47 (1999) 1437–1457, http://dx.doi.org/10.1016/S0022-5096(98)00116-1.

[30] H.N.G. Wadley, N.A. Fleck, A.G. Evans, Fabrication and structural performance of periodic cellular metal sandwich structures, Compos. Sci. Technol. 63 (2003) 2331–2343, http://dx.doi.org/10.1016/S0266-3538(03)00266-5.

[31] L. Wang, M.C. Boyce, C.-Y. Wen, E.L. Thomas, Plastic dissipation mechanisms in periodic Microframe-structured polymers, Adv. Funct. Mater. 19 (2009) 1343–1350, http://dx.doi.org/10.1002/adfm.200801483.

[32] J.H. Lee, L. Wang, S. Kooi, M.C. Boyce, E.L. Thomas, Enhanced energy dissipation in periodic epoxy nanoframes, Nano Lett. 10 (2010) 2592–2597, http://dx.doi.org/10.1021/nl1012773.

[33] S. Shan, S.H. Kang, J.R. Raney, P. Wang, L. Fang, F. Candido, J.A. Lewis, K. Bertoldi, Multistable Architected Materials for Trapping Elastic Strain Energy, Adv. Mater. 27 (2015) 4296–4301, http://dx.doi.org/10.1002/adma.201501708.

[34] T. Frenzel, C. Findeisen, M. Kadic, P. Gumbsch, M. Wegener, Tailored buckling microlattices as reusable light-weight shock absorbers, Adv. Mater. (2016) 5865–5870, http://dx.doi.org/10.1002/adma.201600160.

[35] C. Findeisen, J. Hohe, M. Kadic, P. Gumbsch, Characteristics of mechanical metamaterials based on buckling elements, J. Mech. Phys. Solids 102 (2017) 151–164, http://dx.doi.org/10.1016/j.jmps.2017.02.011.

[36] T.A. Schaedler, C.J. Ro, A.E. Sorensen, Z. Eckel, S.S. Yang, W.B. Carter, A.J. Jacobsen, Designing metallic microlattices for energy absorber applications, Adv. Eng. Mater. 16 (2014) 276–283, http://dx.doi.org/10.1002/adem.201300206.

[37] L. Salari-Sharif, T.A. Schaedler, L. Valdevit, Energy dissipation mechanisms in hollow metallic microlattices, J. Mater. Res. 29 (2014) 1755–1770, http://dx.doi.org/10.1557/jmr.2014.226.

[38] K.J. Maloney, C.S. Roper, A.J. Jacobsen, W.B. Carter, L. Valdevit, T.A. Schaedler, Microlattices as architected thin films: Analysis of mechanical properties and high strain elastic recovery, APL Mater. 1 (2013) 22106 http://dx.doi.org/10.1063/1.4818168.

[39] C.S. Andreasen, E. Andreassen, J.S. Jensen, O. Sigmund, On the realization of the bulk modulus bounds for two-phase viscoelastic composites, J. Mech. Phys. Solids 63 (2014) 228–241, http://dx.doi.org/10.1016/j.jmps.2013.09.007.

[40] D. Jalocha, A. Constantinescu, R. Neviere, Revisiting the identification of generalized Maxwell models from experimental results, Int. J. Solids Struct. 67–68 (2015) 169–181, http://dx.doi.org/10.1016/j.ijsolstr.2015.04.018.

[41] L.J. Gibson, M.F. Ashby, The Mechanics of Three-Dimensional Cellular Materials, Proc. R. Soc. A Math. Phys. Eng. Sci. 382 (1982) 43.

[42] A. Schroer, J. Bauer, R. Schwaiger, O. Kraft, Optimizing the mechanical properties of polymer resists for strong and light-weight micro-truss structures, Extrem. Mech. Lett. 8 (2016) 283–291, http://dx.doi.org/10.1016/j.eml.2016.04.014.

[43] H.F. Brinson, L.C. Brinson, Polymer Engineering Science and Viscoelasticity, (2015), http://dx.doi.org/10.1007/978-1-4899-7485-3.

[44] M.F. Ashby, Materials Selection in Mechanical Design, (2005), http://dx.doi.org/10.1016/B978-1-85617-663-7.00011-4.

[45] M.F. Ashby, A. Evans, N.A. Fleck, L.J. Gibson, J.W. Hutchinson, H.N. Wadley, Metal foams: a design guide, Mater. Des. 23 (119) (2002), http://dx.doi.org/10.1016/S0261-3069(01)00049-8.

[46] N.J. Mills, A. Gilcrist, Creep and recovery of polyolefin foams − deformation mechanisms, J. Cell. Plast. 33 (1997) 264–292, http://dx.doi.org/10.1177/0021955X9703300305.

[47] L.R. Meza, A.J. Zelhofer, N. Clarke, A.J. Mateos, D.M. Kochmann, J.R. Greer, Resilient 3D hierarchical architected metamaterials, Proc. Natl. Acad. Sci. 112 (2015) 11502–11507, http://dx.doi.org/10.1073/pnas.1509120112.

[48] S. Ushiba, K. Masui, N. Taguchi, T. Hamano, S. Kawata, S. Shoji, Size dependent nanomechanics of coil spring shaped polymer nanowires, Sci. Rep. 5 (2015) 17152, http://dx.doi.org/10.1038/srep17152.